Applied Physics A (2018) 124:338
https://doi.org/10.1007/s00339-018-1757-4

Applied Physics A
Materials Science & Processing

Dielectric properties of $(K_{0.5}Na_{0.5})NbO_3$–$(Bi_{0.5}Li_{0.5})ZrO_3$ lead-free ceramics as high-temperature ceramic capacitors

Tianxiang Yan[1,2,3] · Feifei Han[1] · Shaokai Ren[1] · Xing Ma[1] · Liang Fang[1] · Laijun Liu[1] · Xiaojun Kuang[1] · Brahim Elouadi[2]

Received: 11 November 2017 / Accepted: 19 March 2018 / Published online: 26 March 2018

Abstract
$(1-x)K_{0.5}Na_{0.5}NbO_3$–$x(Bi_{0.5}Li_{0.5})ZrO_3$ (labeled as $(1-x)$KNN–xBLZ) lead-free ceramics were fabricated by a solid-state reaction method. A research was conducted on the effects of BLZ content on structure, dielectric properties and relaxation behavior of KNN ceramics. By combining the X-ray diffraction patterns with the temperature dependence of dielectric properties, an orthorhombic–tetragonal phase coexistence was identified for $x=0.03$, a tetragonal phase was determined for $x=0.05$, and a single rhombohedral structure occurred at $x=0.08$. The 0.92KNN–0.08BLZ ceramic exhibits a high and stable permittivity (~1317, ±15% variation) from 55 to 445 °C and low dielectric loss (≤6%) from 120 to 400 °C, which is hugely attractive for high-temperature capacitors. Activation energies of both high-temperature dielectric relaxation and dc conductivity first increase and then decline with the increase of BLZ, which might be attributed to the lattice distortion and concentration of oxygen vacancies.

1 Introduction

The materials with perovskite structure have been extensively investigated due to their interesting dielectric, ferroelectric, pyroelectric and piezoelectric properties for applications in a variety of electronic devices [1–3]. Some particular industries including automotive, aerospace and deep oil well logging have expressed the demands for high-temperature ceramic capacitors (HTCC), which require that the HTCC can possess a high permittivity, low dielectric loss and good dielectric temperature stability at the operating temperature more than 200 °C [4–8]. A typical temperature involving capacitors on the wheel is required to work as high as 250 °C, and the temperature is 200–300 °C in the cylinder [4]. The filter capacitors in silicon carbide power invertor are generally in need of operating beyond 200 °C [6]. The $BaTiO_3$-based dielectrics with high permittivity have been widely used as capacitors for many years [9]. However, their operating temperatures are normally insufficient high due to the low Curie temperature (T_C) of $BaTiO_3$ (~120 °C) [10–12].

$K_{0.5}Na_{0.5}NbO_3$ (KNN) ceramics possess a potential for high-temperature applications because of the high T_C of this system [13]. However, the dielectric peaks at ~200 °C (T_{O-T}) and ~410 °C (T_C) corresponding to orthorhombic–tetragonal (O–T) and tetragonal–cubic (T–C) phase transitions deteriorate the dielectric temperature stability [14]. To overcome the performance deterioration near phase transitions, an alternative way of developing high-temperature KNN-based dielectrics is to form relaxor ferroelectrics with a relative flat permittivity in a wide temperature range by introducing modified compositions or dopants [15–19].

Recently, relaxor behavior has been found in KNN–$AZrO_3$ binary system, such as $(1-x)$KNN–$x$$SrZrO_3$ [20], $(1-x)$KNN–$x$$BaZrO_3$ [21], and $(1-x)$KNN–$x(Bi_{0.5}Na_{0.5})ZrO_3$

✉ Laijun Liu
ljliu2@163.com

✉ Xiaojun Kuang
kuangxj@glut.edu.cn

✉ Brahim Elouadi
belouadi@univ-lr.fr

[1] Guangxi Universities Key Laboratory of Non-ferrous Metal Oxide Electronic Functional Materials and Devices, College of Materials Science and Engineering, College of Mechanical and Control Engineering, Guilin University of Technology, Guilin 541004, China

[2] Laboratory of Chemical Analysis Elaboration and Materials, Engineering (LEACIM), Université de La Rochelle, Avenue Michel Crépeau, 17042 La Rochelle Cedex 01, France

[3] Guangxi Scientific Experiment Center of Mining, Metallurgy and Environment, Guilin University of Technology, Guilin 541004, China

[22]. Permittivity peaks in KNN–$AZrO_3$ system become much broader than that in undoped KNN, resulting in an enhanced permittivity temperature stability and an extended temperature usage range. Unfortunately, the *Tc* declines hugely with the addition of compositions, and consequently limits the high-temperature applications. Moreover, it was reported by Naama Klein et al. [23] that Li substitution at A site of KNN could shift T_C to high temperatures. In addition, previous studies showed that the addition of Bi^{3+} could effectively improve the electrical properties of KNN ceramics [24, 25]. However, there is few investigation on the influence of $(Bi_{0.5}Li_{0.5})ZrO_3$ content on the high-temperature dielectric properties of KNN.

In this study, $(Bi_{0.5}Li_{0.5})ZrO_3$ was selected to modify the structure and properties of KNN. In addition, dielectric behavior of the system was focused on to disclose the high-temperature dielectric loss mechanism by impedance spectroscopy.

2 Experimental procedures

$(1-x)K_{0.5}Na_{0.5}NbO_3$–$x(Bi_{0.5}Li_{0.5})ZrO_3$ (labeled as $(1-x)$KNN–xBLZ, $x=0.00$, 0.03, 0.05 and 0.08) lead-free ceramics were fabricated via the solid-state reaction route. Starting materials K_2CO_3 (99%), Na_2CO_3 (99.8%), Li_2CO_3 (98%), Nb_2O_5 (99.99%), ZrO_2 (99%) and Bi_2O_3 (99%) were dried at 120 °C for 24 h before weighting. The dried powders were thoroughly weighted according to the stoichiometric ratio and mixed using a planetary mill for 8 h. The mixture was calcined at 900 °C for 4 h and mixed again using a planetary mill for 8 h. The calcined powder was granulated with 5 wt% PVA as a binder and then pressed under ~ 350 MPa into discs of 12 mm in diameter and ~ 1.2 mm in thickness. The discs with different BLZ content were sintered in a temperature range of 1100–1140 °C for 4 h in air.

Ceramic density was measured by the Archimedes method. Typical X-ray diffraction (XRD) patterns of the $(1-x)$KNN–xBLZ ceramics were obtained by an automated diffractometer (X'Pert PRO, PANalytical) with Cu K_α ($\lambda=1.5418$ Å) radiation at room temperature. For dielectric measurement, the sintered discs were polished into about 1 mm in thickness. Silver paste electrodes were coated at both surfaces of the samples and fired at 650 °C for 0.5 h. The permittivity on elevated temperature was taken using a precision impedance analyzer (Agilent 4294A) in the temperature range of 30–550 °C varied in 3 °C. The Rietveld refinements were performed using the GSAS-EXPGUI software. The space groups, cell parameters, and atom positions were selected according to the reference [26]. The scaling ratio, zero point, background, cell parameters, atom positions, isotropic displacement parameters and profile shape parameters were fitted during the refinement.

3 Results and discussion

XRD patterns of the $(1-x)$KNN–xBLZ ceramics at room temperature (RT) are plotted in Fig. 1. A small amount of secondary phase ($K_2Nb_4O_{11}$) is detected for undoped KNN by X'Pert HighScore Plus software. With the addition of BLZ, the secondary phase disappears and single perovskite structure is obtained for the samples with $x \geq 0.03$, which suggests that BLZ could efficiently suppress the secondary phase as a fine sintering aid. Moreover, it is noticeable that the increase of BLZ gradually changes crystal symmetry of the ceramics. Undoped KNN exhibits an orthorhombic structure (Amm2) at RT, which could be confirmed by splitting of (022) and (200) diffraction peaks near 2θ of 45° and higher relative intensity of the (022) peak. With increasing BLZ, the (022) peak is depressed and the relative intensity of (200) peak increased, thus a typical O–T mixed phase is detected in the $x=0.03$ sample. Further addition of BLZ leads to the suppression of orthorhombic phase, and then the tetragonal phase (P4mm) with higher relative intensity of (200) peak occurs at the sample of $x=0.05$ [27–31]. Subsequently, two peaks gradually merges into a symmetric peak corresponding to (200) peak for $x=0.08$, implying appearance of a rhombohedral phase (R3m) in agreement with $BaZrO_3$ modified KNN [21].

Lattice parameter of all samples was determined using Rietveld refinement software (GSAS-EXPGUI) [27] based on X-ray diffraction data and listed in Table 1. The unit cell parameter decreases with the addition of BLZ, which could be ascribed to ionic substitution. For $(1-x)$KNN–xBLZ solid solution, since $(Bi_{0.5}Li_{0.5})^{2+}$ for $(K_{0.5}Na_{0.5})^{+}$ displaces A site while Zr^{4+} for Nb^{5+} locates at B site, the size of $(Bi_{0.5}Li_{0.5})^{2+}$ (1.30 Å, CN = 12) is much smaller than that of $(K_{0.5}Na_{0.5})^{+}$ (1.515 Å, CN = 12) in contrast with the larger

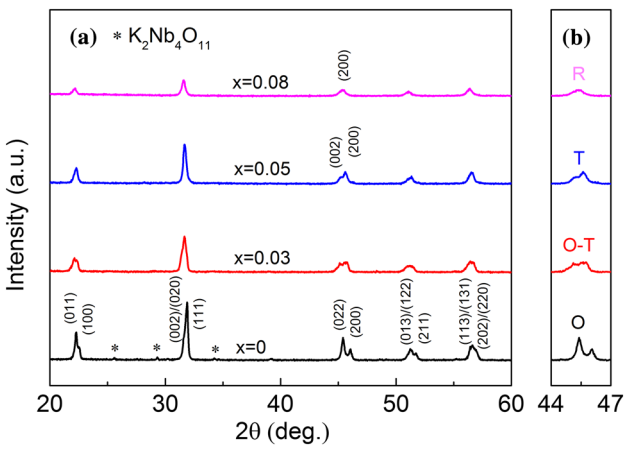

Fig. 1 XRD patterns of the $(1-x)$KNN–xBLZ ceramics at room temperature

Table 1 Phase, lattice parameters, cell volume, and relative density of the $(1-x)$ KNN–xBLZ ceramics

Composition	Phase	a (Å)	b (Å)	c (Å)	V (Å^3)	Relative density (%)
$x=0$	Orthorhombic (Amm2)	3.9601	5.6561	5.6816	127.256	92.9
$x=0.03$	Orthorhombic (Amm2) + tetragonal (P4mm)	3.9585 3.9721	5.6455 3.9721	5.6721 4.0190	126.755 63.408	94.6
$x=0.05$	Tetragonal (P4mm)	3.9698	3.9698	3.9998	63.036	96.4
$x=0.08$	Rhombohedral (R3m)	3.9718	3.9718	3.9718	62.640	94.9

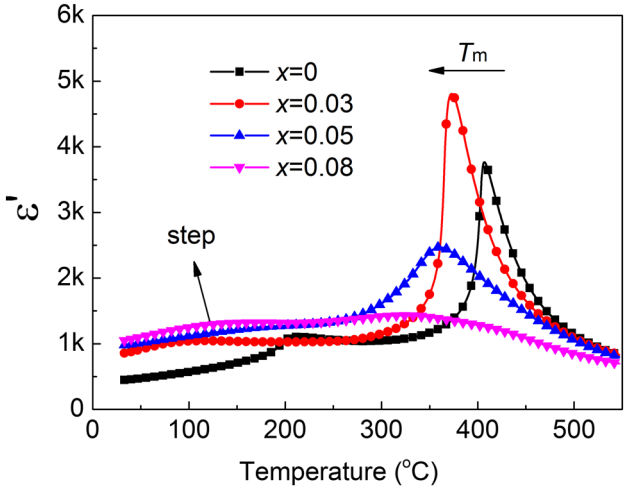

Fig. 2 Temperature dependence of permittivity (ε') for the $(1-x)$ KNN–xBLZ ceramics at 1 MHz

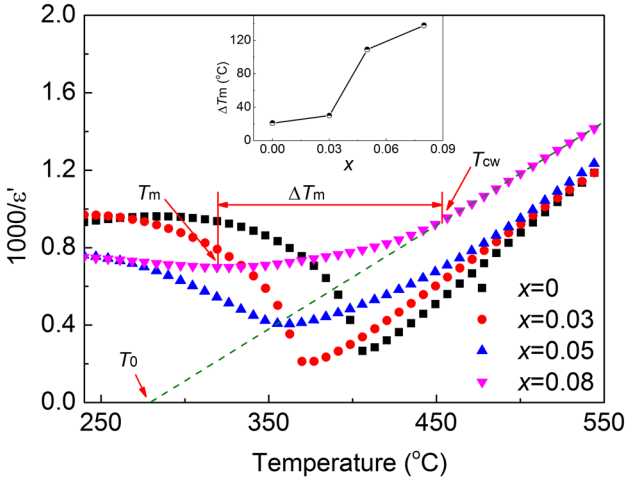

Fig. 3 The reciprocal of permittivity for the $(1-x)$KNN–xBLZ ceramics at 1 MHz as a function of temperature

size of Zr^{4+} (0.72 Å, CN = 6) than that of Nb^{5+} (0.64 Å, CN = 6) [32, 33]. Great lattice distortion is present with the increase of BLZ. Furthermore, the larger size ions at B site could enhance the stability of rhombohedral phase, which is in agreement with the XRD results.

Figure 2 depicts temperature dependence of permittivity (ε') for the $(1-x)$KNN–xBLZ ceramics at 1 MHz. For undoped KNN with orthorhombic structure at RT, two permittivity peaks corresponding to T_{O-T} and T_C above RT can be seen clearly. With the addition of BLZ, both T_{O-T} and T_C dramatically shift to lower temperatures, while the T_{O-T} around RT can be observed in the $x=0.03$ sample, which suggests the O–T mixed phase is present at RT in agreement with the XRD results [23, 31]. Further increasing BLZ, the T_{O-T} disappears while only T_C exists above RT in the composition of $x=0.05$. For $x=0.08$, it is found that permittivity peak exhibits a step-like behavior near RT, which could be ascribed to increase of rhombohedral–tetragonal (R–T) transition in correspondence with the dielectric behavior reported in KNN-based system [34, 35]. All results further verify crystal symmetry of the $(1-x)$KNN–xBLZ ceramics, which is consistent with the XRD analysis. Moreover, it is noticeable that the T–C transition peaks are sharp for the compositions with $x=0$ and 0.03, while for the samples of $x=0.05$ and 0.08, the transition peak becomes much broader and shows an apparent characteristic of relaxor behavior with the diffuse phase transition.

To further quantitatively characterize the relaxor behavior of diffuse phase transition for the $(1-x)$KNN–xBLZ system, the characterizations of relaxor behavior have been described. The permittivity of normal ferroelectrics above Curie point (T_c) obeys the Curie–Weiss law as follows [36]:

$$1/\varepsilon' = (T - T_0)/C \quad (T > T_C), \tag{1}$$

where C is the Curie–Weiss constant which can reflect the nature of ferroelectric transition, and T_0 is the Curie–Weiss temperature. Figure 3 shows the reciprocal of permittivity for the $(1-x)$KNN–xBLZ ceramics at 1 MHz as a function of temperature. It is clear that permittivity deviates from the Curie–Weiss law for the samples with $x \geq 0.05$. The deviation degree (ΔT_m) from the Curie–Weiss law can be defined as [36]:

$$\Delta T_m = T_{CW} - T_m \tag{2}$$

where T_{CW} is the temperature at which the permittivity begins to deviate from the Curie–Weiss law and T_m is the temperature at permittivity maxima as shown in Fig. 3. The perfect linear fittings above T_{CW} are obtained and the best

Table 2 Curie–Weiss temperature (T_0), Curie–Weiss constant (C), temperature at which the permittivity starts to deviate from the Curie–Weiss law (T_{CW}), temperature at the maximum of permittivity (T_m), deviation degree (ΔT_m) and diffuse factor (γ) for the $(1-x)$ KNN–xBLZ ceramics at 1 MHz

Composition	$x=0$	$x=0.03$	$x=0.05$	$x=0.08$
T_o (°C)	378	351	343	279
$C\times10^5$ (°C)	1.40	1.63	1.64	1.87
T_{CW} (°C)	428	403	469	458
T_m (°C)	407	373	360	320
$\Delta T_m = T_{CW} - T_m$ (°C)	21	30	109	138
γ	1.25	1.40	1.62	1.94

fitting parameters are listed in Table 2. The inset of Fig. 3 shows that ΔT_m increases with the addition of BLZ. It suggests that the diffuse phase transition behavior of the $(1-x)$ KNN–xBLZ system is evidently enhanced by introducing BLZ.

Generally, the diffuseness of phase transition for relaxor ferroelectrics with diffuse phase transition follows a modified Curie–Weiss law as depicted by [37]:

$$\frac{1}{\varepsilon'} - \frac{1}{\varepsilon'_m} = \frac{(T - T_m)^\gamma}{C}, \quad (3)$$

where ε'_m is the permittivity maxima, C is the Curie–Weiss constant, and γ $(1 \le \gamma \le 2)$ is the diffuse factor. Generally, $\gamma = 1$ and $\gamma = 2$ present the Curie–Weiss behavior for normal ferroelectrics and classical relaxor ferroelectrics, respectively [37]. To further verify the effect of the BLZ on the phase transition behavior of KNN, the plots of $\log(1/\varepsilon' - 1/\varepsilon'_m)$ versus $\log(T - T_m)$ for the $(1-x)$ KNN–xBLZ ceramics at 1 MHz are displayed in Fig. 4. The γ can be obtained from the slope of linear fitting as shown by solid lines in Fig. 4. It is found that γ increases monotonously from 1.25 to 1.94 with the addition of BLZ, implying that the $(1-x)$KNN–xBLZ ceramics change from normal ferroelectrics to relaxor ferroelectrics. Generally, ionic substitutions [i.e., $(Bi_{0.5}Li_{0.5})^{2+}$ for $(K_{0.5}Na_{0.5})^{+}$ at A site and Zr^{2+} for Nb^{5+} at B site] give rise to size and valence mismatches. $Nb^{5+}$and Zr^{4+} have ionic radii of 0.64 and 0.72 Å, respectively. A more pronounced off-center shift of the smaller Nb atoms is observed in their oxygen octahedral cage in comparison to the larger Zr atom. Then, the substitutions of K^+/Na^+ with Li^+/Bi^{3+} (exhibiting a stereochemically active lone electron pair) and Nb^{5+} with Zr^{4+} not only disturbs the long-range Nb^{5+} displacement, but also results in substantial local lattice strain. Local size mismatch could produce random strains, while local valence mismatch could result in quenched random electric fields (RFs). The RFs hinder long-range ferroelectric ordering and generate polar nano-regions (PNRs) [38, 39]. The existence of PNRs has

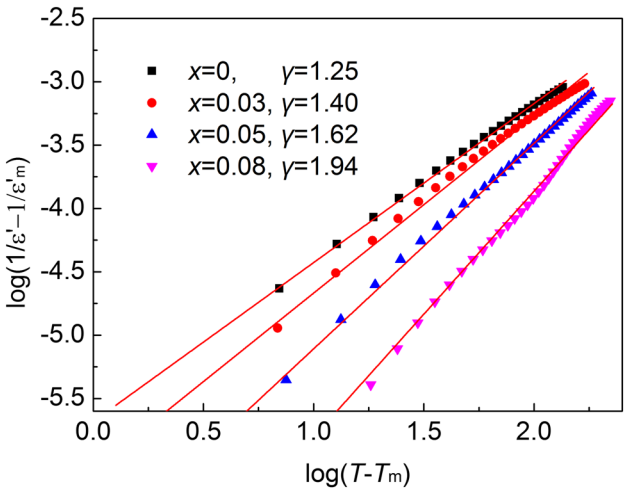

Fig. 4 $\text{Log}(1/\varepsilon' - 1/\varepsilon'_m)$ as a function of $\log(T - T_m)$ for the $(1-x)$ KNN–xBLZ ceramics at 1 MHz with various BLZ content. The red solid lines is the linear fittings according to Eq. (3)

been confirmed by the neutron elastic diffuse scattering and TEM in PMN relaxor ferroelectric [40, 41]. When the substitution concentration is not very high, the PNRs are isolated and embedded in the $(1-x)$KNN–xBLZ ceramics matrix, which lead to the relaxor behavior.

Figure 5 presents temperature coefficient curves of permittivity $(\Delta\varepsilon'/\varepsilon'_{200°C},\ \Delta\varepsilon' = \varepsilon' - \varepsilon'_{200°C})$ and dielectric loss ($\tan\delta$) as a function of temperature for the $(1-x)$ KNN–xBLZ ceramics at 1 MHz. In Fig. 5a, the temperature coefficient curve of the permittivity near T_c is hugely influenced by the addition of BLZ. Particularly, the composition with $x = 0.08$ exhibits a high and stable permittivity (~1317) from 55 to 445 °C based on ± 15% variation, which is the tolerance of electronic industries alliance (EIA) X8R/X9R capacitors assigned currently for operating at elevated temperatures [8]. Moreover, it is found from Fig. 3b that low $\tan\delta$ (≤ 0.06) extends from 120 to 400 °C. Therefore, the 0.92KNN–0.08BLZ ceramic is hugely attractive for high-temperature capacitors. However, $\tan\delta$ of the samples increases hugely at higher temperatures due to a thermally activated conductivity [42].

Impedance spectroscopy is usually utilized to study the dielectric behavior of ceramic materials [43]. To further understand high-temperature dielectric loss behavior of the samples, normalized imaginary parts of impedance for the $(1-x)$KNN–xBLZ ceramics as a function of frequency at measured temperatures are plotted in Fig. 6. Each curve of the samples at given temperatures exhibits a symmetric peak with a frequency maximum (relaxation frequency). The relaxation frequency gradually shifts to the higher frequency side with the increase of temperature. It suggests a thermally activated relaxation behavior. The relation between relaxation frequency and temperature follows the Arrhenius law:

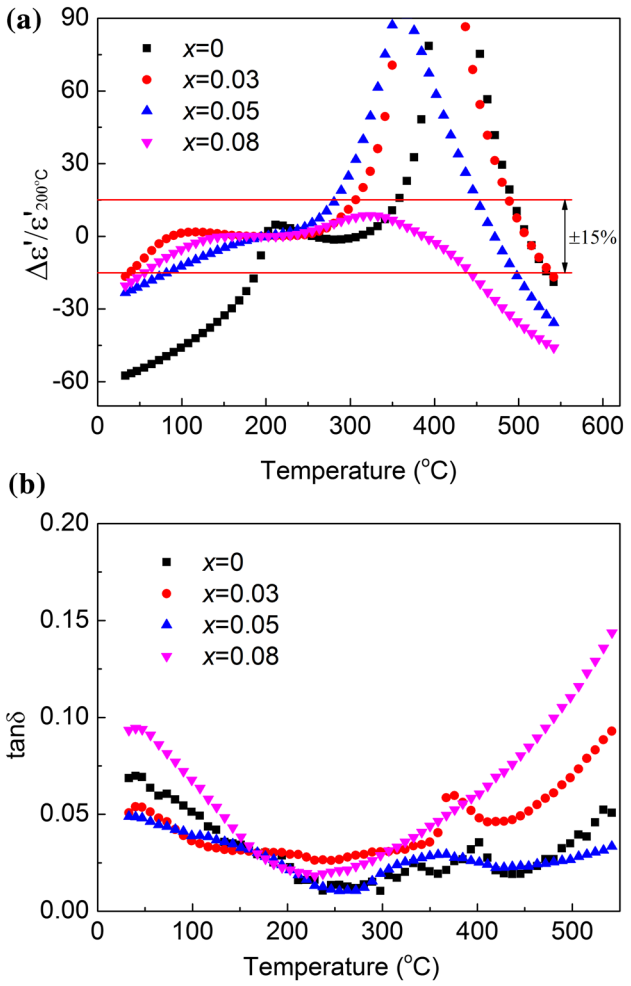

Fig. 5 Temperature coefficient of permittivity (**a**) and dielectric loss (**b**) as a function of temperature for the $(1-x)$KNN–xBLZ ceramics at 1 MHz

$$f_{\max} = f_0 \exp\left(\frac{-E_{\mathrm{rel}}}{k_{\mathrm{B}}T}\right), \tag{4}$$

where $f_{\max}$ is the relaxation frequency, f_0 is the pre-exponential factor, E_{rel} is the activation energy of relaxation, k_{B} and T are the Boltzmann constant and measured Kelvin temperature, respectively. From the slope of the straight lines obtained from ln ($f_{\max}$) versus (1000/T) plots in Fig. 7, the E_{rel} can be calculated: $E_{\mathrm{rel}} = 1.009$ eV for $x = 0$, $E_{\mathrm{rel}} = 1.014$ eV for $x = 0.03$, $E_{\mathrm{rel}} = 1.627$ eV for $x = 0.05$ and $E_{\mathrm{rel}} = 1.106$ eV for $x = 0.08$. The E_{rel} first increases then declines with increasing BLZ.

Figure 8 plots ac conductivity (σ_{ac}) of the $(1-x)$KNN–xBLZ ceramics as a function of frequency at measured temperatures. The σ_{ac} of all samples declines with the decrease of frequency, and then exhibits a fixed value close to dc conductivity at low frequencies. This conductivity behavior normally obeys the "universal dielectric response" (UDR) law [44]:

$$\sigma_{\mathrm{ac}} = \sigma_{\mathrm{dc}} + \sigma_0 f^s, \tag{5}$$

where σ_{dc} is the dc conductivity, σ_0 is pre-exponential factor, f and s are the frequency and exponential term ($0 < s \leq 1$). The UDR law depicts one phenomenon connected with many-body interactions between charges and dipoles. The perfect fittings between σ_{ac} and frequency with Eq. (5) as shown by solid lines in Fig. 8 are carried out to achieve σ_{dc} values at different temperatures. The relation between obtained σ_{dc} and temperature obeys the Arrhenius law:

$$\sigma_{\mathrm{dc}} = T^{-1}\sigma_0 \exp\left(-\frac{E_{\mathrm{con}}}{k_{\mathrm{B}}T}\right), \tag{6}$$

where σ_0 is pre-exponential factor, E_{con} is the activation energy of dc conductivity, k_{B} and T are the Boltzmann constant and measured Kelvin temperature, respectively. From the slope of straight lines obtained from ln ($T\,\sigma_{\mathrm{dc}}$) versus (1000/T) plots in Fig. 9, the E_{con} can be calculated: $E_{\mathrm{con}} = 0.634$ eV for $x = 0$, $E_{\mathrm{con}} = 0.644$ eV for $x = 0.03$, $E_{\mathrm{con}} = 1.246$ eV for $x = 0.05$ and $E_{\mathrm{con}} = 0.864$ eV for $x = 0.08$. The E_{con} first increases then declines with increasing BLZ, which agrees with the variation of E_{rel}. It has been reported that the activation energies for single- and doubly ionized oxygen vacancies are in the range of 0.3–0.5 and 0.6–1.2 eV in perovskite oxides, respectively [42, 44]. Thus, both E_{rel} and E_{con} for the $(1-x)$KNN–xBLZ ceramics should be related to the doubly ionized oxygen vacancies.

It is known that the volatilization of K/Na/Li/Bi during sintering gives rise to oxygen vacancies, meanwhile the possible Nb^{5+} substitution by Zr^{4+} occurs, as described in the Kroger–Vink notation by Eq. (7–9):

$$A_{\mathrm{A}} \rightarrow A + V'_{\mathrm{A}} + \frac{1}{2}V_O^{\bullet\bullet}, \tag{7}$$

$$\mathrm{Bi}_{\mathrm{Bi}} \rightarrow \mathrm{Bi} + V'''_{\mathrm{Bi}} + \frac{3}{2}V_{\mathrm{O}}^{\bullet\bullet}, \tag{8}$$

$$\mathrm{Zr}_{\mathrm{Zr}} \rightarrow \mathrm{Zr}'_{\mathrm{Nb}} + \frac{1}{2}V_{\mathrm{O}}^{\bullet\bullet}, \tag{9}$$

where V'_{A} is vacancies of K/Na/Li, $V_{\mathrm{O}}^{\bullet\bullet}$ is the doubly ionized oxygen vacancy, V'''_{Bi} is the Bi vacancy, and $\mathrm{Zr}'_{\mathrm{Nb}}$ is the quadruply ionized Zr^{4+} which occupies at the Nb^{5+} site. Since one Bi vacancy induces more oxygen vacancies than that of K/Na/Li and the compensated oxygen vacancies is formed due to the creation of the negatively charged defect $\mathrm{Zr}'_{\mathrm{Nb}}$, the high concentration of oxygen vacancies results in the decrease of activation energy with increasing BLZ. In this work, why do both E_{rel} and E_{con} first increases and then decrease with the increase of BLZ? Considering the change of lattice parameter for the $(1-x)$KNN–xBLZ system as

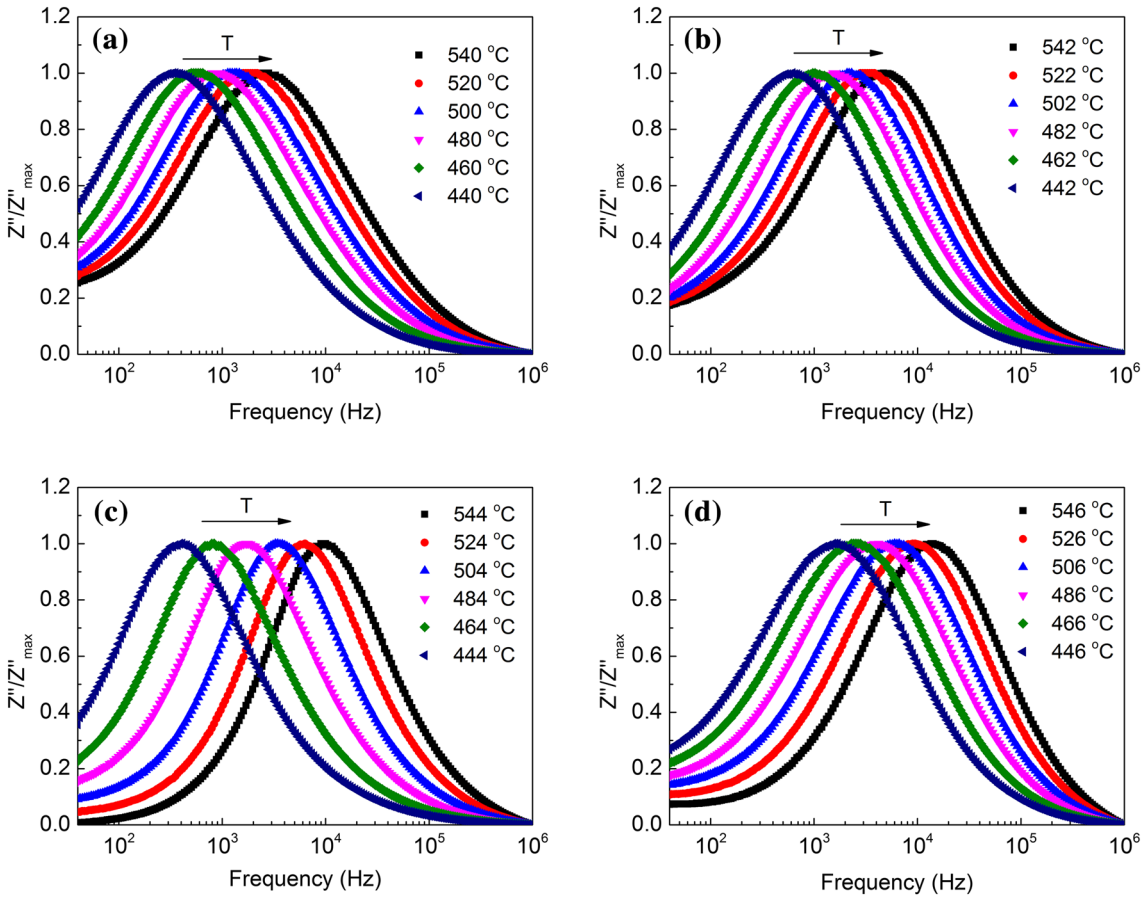

Fig. 6 Normalized imaginary parts of impedance for the $(1-x)$KNN–xBLZ ceramics as a function of frequency at measured temperatures, **a** $x=0$, **b** $x=0.03$, **c** $x=0.05$, **d** $x=0.08$

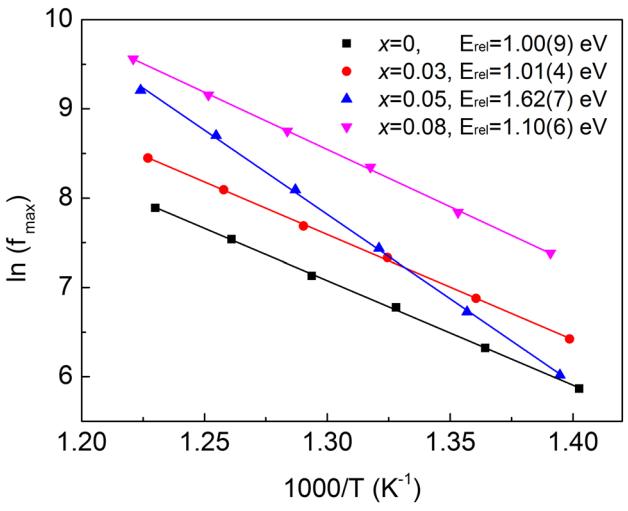

Fig. 7 Arrhenius plots of relaxation frequency (f_{max}) for the $(1-x)$KNN–xBLZ ceramics. The symbols are the experimental data and the solid lines are the linear fittings according to Eq. (4)

mentioned above, it is assumed that the magnitude of activation energy could be associated with both lattice distortion and the concentration of oxygen vacancies. With the addition of BLZ, lattice parameter of the samples of $x=0.03$ and 0.05 dramatically drops due to the change of crystal symmetry, and the higher energy barrier for oxygen vacancies hopping results in the increase of activation energy [45]. Further increasing BLZ, the lattice parameter of the sample of $x=0.08$ slightly decreases, and the enhanced concentration of oxygen vacancies plays a dominant role on the decrease of activation energy.

4 Conclusions

$(1-x)K_{0.5}Na_{0.5}NbO_3$–$xBi_{0.5}Li_{0.5}O_3$ ceramics were prepared by the solid-state reaction method. The stability of rhombohedral phase and relaxor behavior are enhanced with the increase of BLZ. The 0.92KNN–0.08BLZ ceramic shows a high and stable permittivity (~ 1317, ± 15% variation) from 55 to 445 °C and low dielectric loss (≤ 6%) from 120 to

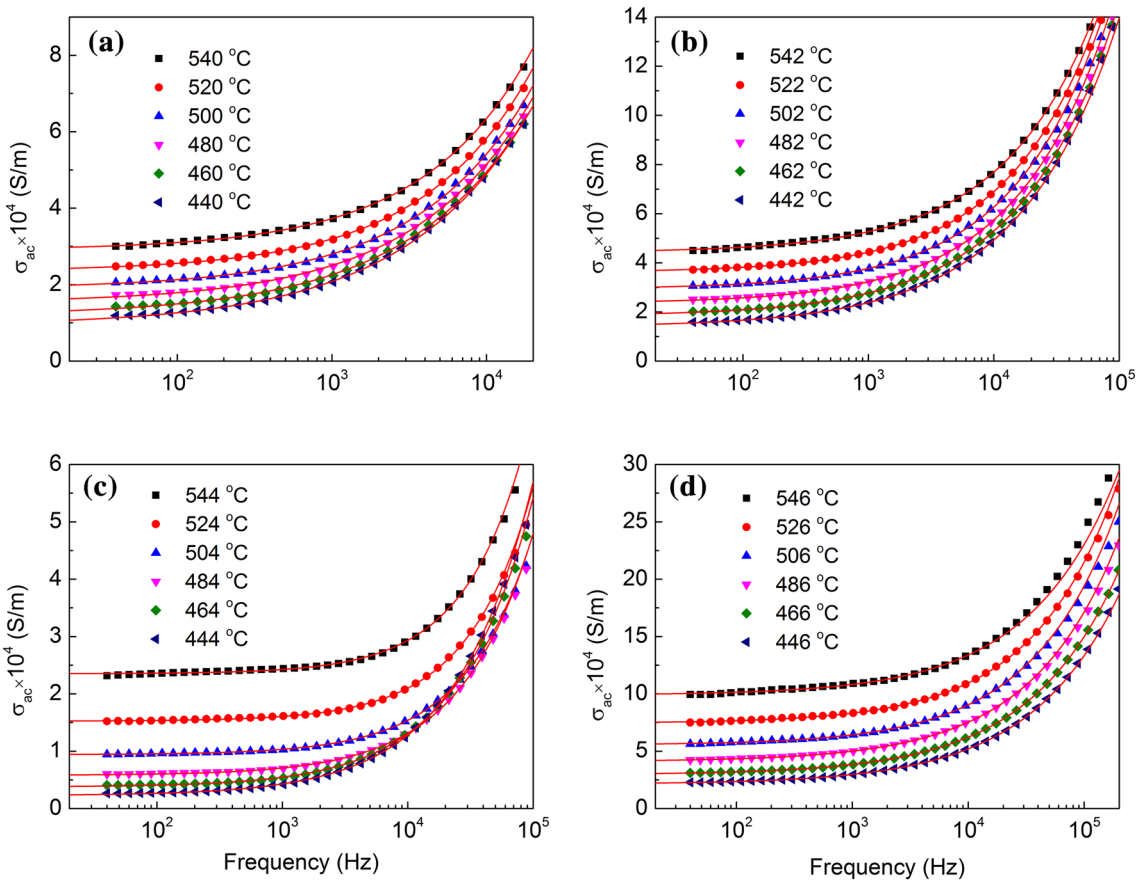

Fig. 8 Ac conductivity (σ_{ac}) of the $(1-x)$KNN–xBLZ ceramics as a function of frequency at measured temperatures, **a** $x=0$, **b** $x=0.03$, **c** $x=0.05$, **d** $x=0.08$. The solid lines are the fittings according to Eq. (5)

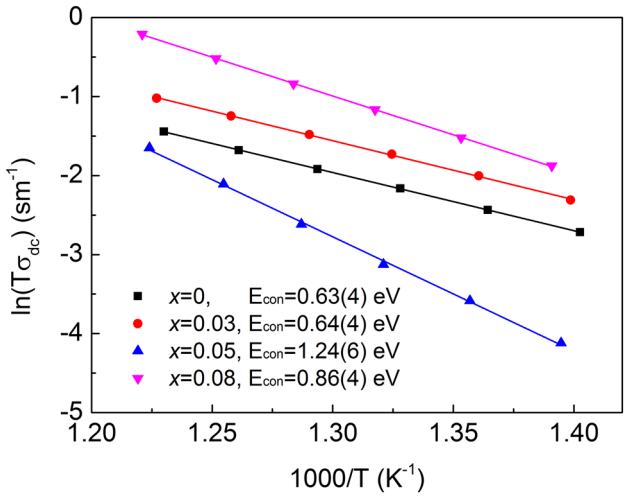

Fig. 9 Arrhenius plots of the dc conductivity for the $(1-x)$KNN–xBLZ ceramics. The symbols are the experimental data and the solid lines are the linear fittings according to Eq. (6)

400 °C, which is hugely attractive for HTCC applications. The high-temperature conduction presents a thermally activated behavior, which might be attributed to lattice distortion and the concentration of oxygen vacancies.

Acknowledgements This work was supported by the National Natural Science Foundation of China (nos. 11264010, 11564010, 51402196), the Natural Science Foundation of Guangxi (GA139008, 2016GXNSFDA380027), and the China Postdoctoral Science Foundation (Grants 2014M552229 and 2015T80915).

References

1. H. Zhang, P. Xu, E. Patterson, J. Zang, S. Jiang, J. Rödel, J. Eur. Ceram. Soc. **35**, 2501 (2015)
2. H. Zhang., S. Jiang, J. Xiao, K. Kajiyoshi, J. Appl. Phys. **107**, 124118 (2010)
3. H. Zhang, S. Jiang, K. Kajiyoshi, J. Xiao, J. Am. Ceram. Soc. **93**, 750 (2010)
4. R.W. Johnson, J.L. Evans, P. Jacobsen, J.R. Thompson, M. Christopher, IEEE Trans. Electron. Packag. Manuf. **27**, 164 (2004)
5. Z. Chen, G. Li, X. Sun, L. Liu, L. Fang, Ceram. Int. **41**, 11057 (2015)
6. J.B. Casady, R.W. Johnson, Solid State Electron. **39**, 1409 (1996)

7. H. Cheng, H. Du, W. Zhou, D. Zhu, F. Luo, B. Xu, J. Am. Ceram. Soc. **96**, 833 (2013)
8. X. Chen, J. Chen, D. Ma, G. Huang, L. Fang, H. Zhou, Mater. Lett. **145**, 247 (2015)
9. H. Kishi, Y. Mizuno, H. Chazono, Jpn. J. Appl. Phys. **42**, 1 (2003)
10. M.J. Pan, C.A. Randall, A. Brief, IEEE Electr. Insul. Mag. **26**, 44 (2010)
11. K. Kobayashi, M. Ryu, Y. Doshida, Y. Mizuno, C.A. Randall, X. Tan, J. Am. Ceram. Soc. **96**, 531 (2013)
12. Z. Zhang, Y. Wu, J. Miao, Z. Liu, Y. Li, Ceram. Int. **41**, S9 (2015)
13. Y. Saito, H. Takao, T. Tani, T. Nanoyama, K. Takatori, T. Homma et al., Nature **123**, 84 (2004)
14. C.C. Wang, J. Wang, X.H. Sun, L.N. Liu, J. Zhang, J. Zheng, C. Cheng, Solid State Commun. **179**, 29 (2014)
15. H.L. Du, W.C. Zhou, F. Luo, J. Appl. Phys. **105**, 124104 (2009)
16. H. Cheng, W. Zhou, H. Du, F. Luo, D. Zhu, D. Jiang, B. Xu, J. Alloy. Comp. **579**, 192 (2013)
17. X. Chen, D. Ma, G. Huang, J. Chen, H. Zhou, Ceram. Int. **41**, 13883 (2015)
18. L. Zhang, S. Wang, F. Liu, J. Electron. Mater. **44**, 3408 (2015)
19. V. Bobnar, J. Holc, M. Hrovat, M. Kosec, J. Appl. Phys. **101**, 074103 (2007)
20. T. Yan, F. Han, S. Ren, J. Deng, X. Ma, L. Ren, L. Fang, L. Liu, B. Peng, B. Elouadi, Mater. Res. Bull. **99**, 403–408 (2018)
21. R.P. Wang, H. Bando, T. Katsumata, Y. Inaguma, H. Taniguchi, M. Itoh, Phys. Status Solidi RRL **3**, 142 (2009)
22. Z. Wang, D. Xiao, J. Wu, M. Xiao, F. Li, J. Zhu, J. Am. Ceram. Soc. **97**, 688 (2014)
23. N. Klein, E. Hollenstein, D. Damjanovic, H. Trodahl, N. Setter, M. Kuball, J. Appl. Phys. **102**, 014112 (2007)
24. H.L. Du, D.J. Liu, F.S. Tang, J. Am. Ceram. Soc. **90**, 2824 (2007)
25. H.L. Du, W.C. Zhou, F. Luo, J. Appl. Phys. **104**, 044104 (2008)
26. A.W. Hewat, J. Phys. C. Solid State Phys. **6**, 2559 (1973)
27. C. Long, T. Li, H. Fan, Y. Wu, L. Zhou, Y. Li, L. Xiao, Y. Li, J. Alloy. Comp. **658**, 839 (2016)
28. R.Z. Zuo, X.S. Fang, C. Ye, Appl. Phys. Lett. **90**, 092904 (2007)
29. L. Liu, M. Knapp, L.A. Schmitt, H. Ehrenberg, L. Fang, H. Fuess, M. Hoelzel, M. Hinterstein, EPL. **114**, 47011 (2016)
30. L. Liu, M. Knapp, H. Ehrenberg, L. Fang, L.A. Schmitt, H. Fuess, M. Hoelzel, M. Hinterstein, J. Appl. Crystallogr. **49**, 574 (2016)
31. L. Liu, M. Knapp, H. Ehrenberg, L. Fang, H. Fan, L.A. Schmitt, H. Fuess, M. Hoelzel, H. Dammak, M. Pham-Thi, M. Hinterstein, J. Euro. Ceram. Soc. **37**, 1387 (2017)
32. D.I. Woodward, I.M. Reaney, R.E. Eitel, C.A. Randall, J. Appl. Phys. **94**, 3313 (2003)
33. R.D. Shannon, Acta Crystallogr. **32**, 751 (1976)
34. W.F. Liang, W.J. Wu, D.Q. Xiao, J.G. Zhu, J.G. Wu, J. Mater. Sci. **46**, 6871 (2011)
35. W.F. Liang, W.J. Wu, D.Q. Xiao, J.M. Zhu, J.G. Zhu, J.G. Wu, Phys. Status Solidi RRL **5**, 220 (2011)
36. Y. Guo, K.I. Kakimoto, H. Ohsato, Solid State Commun. **129**, 279 (2004)
37. K. Uchino, S. Nomura, Ferroelectr. Lett. Sect. **44**, 55 (1982)
38. A.A. Bokov, Z.G. Ye, J. Mater. Sci. **41**, 31 (2006)
39. L. Liu, X. Ma, M. Knapp, H. Ehrenberg, L. Fang, M. Hinterstein, EPL. **118**, 47001 (2017)
40. G. Xu, G. Shirane, J.R.D. Copley, P.M. Gehring, Phys. Rev. B **69**, 064112 (2004)
41. M. Yoshida, S. Mori, N. Yamamoto, Y. Uesu, J.M. Kiat, Ferroelectrics **217**, 327 (1998)
42. L. Liu, Y. Huang, C. Su, L. Fang, M. Wu, C. Hu, H. Fan, Appl. Phys. A **104**, 1047 (2011)
43. J. Zang, M. Li, D. Sinclair, W.J.J. Rödel, J. Am. Ceram. Soc. **97**, 1523 (2014)
44. T. Yan, X. Sun, J. Deng, S. Liu, F. Han, X. Liu, L. Fang, D. Lin, B. Peng, L. Liu, Solid State Commun. **264**, (2017)
45. A. Molak, E. Ksepko, I. Gruszka, A. Ratuszna, M. Paluch, Z. Ujma, Solid State Ion. **176**, 1439 (2005)